

## MODELING THE OPTICAL – X-RAY ACCRETION LAG IN LMC X-3: INSIGHTS INTO BLACK-HOLE ACCRETION PHYSICS

JAMES F. STEINER<sup>1†</sup>, JEFFREY E. MCCLINTOCK<sup>1</sup>, JEROME A. OROSZ<sup>2</sup>, MICHELLE M. BUXTON<sup>3</sup>, CHARLES D. BAILYN<sup>3</sup>, RONALD A. REMILLARD<sup>4</sup>, AND ERIN KARA<sup>5</sup>*Draft version January 23, 2014*

## ABSTRACT

The X-ray persistence and characteristically soft spectrum of the black hole X-ray binary LMC X-3 make this source a touchstone for penetrating studies of accretion physics. We analyze a rich, 10-year collection of optical/infrared (OIR) time-series data in conjunction with all available contemporaneous X-ray data collected by the ASM and PCA detectors aboard the *Rossi X-ray Timing Explorer*. A cross-correlation analysis reveals an X-ray lag of  $\approx 2$  weeks. Motivated by this result, we develop a model that reproduces the complex OIR light curves of LMC X-3. The model is comprised of three components of emission: stellar light; accretion luminosity from the outer disk inferred from the time-lagged X-ray emission; and light from the X-ray-heated star and outer disk. Using the model, we filter a strong noise component out of the ellipsoidal light curves and derive an improved orbital period for the system. Concerning accretion physics, we find that the local viscous timescale in the disk increases with the local mass accretion rate; this in turn implies that the viscosity parameter  $\alpha$  decreases with increasing luminosity. Finally, we find that X-ray heating is a strong function of X-ray luminosity below  $\approx 50\%$  of the Eddington limit, while above this limit X-ray heating is heavily suppressed. We ascribe this behavior to the strong dependence of the flaring in the disk upon X-ray luminosity, concluding that for luminosities above  $\approx 50\%$  of Eddington, the star lies fully in the shadow of the disk.

*Subject headings:* black hole physics — accretion, accretion disks — X-rays: binaries

## 1. INTRODUCTION

LMC X-3 was one of the first extragalactic X-ray sources to be discovered (Leong et al. 1971). It was subsequently identified with a B main-sequence star (Jones et al. 1974; Johnston et al. 1979). With the discovery that the star is in a 1.7-day binary orbit with a massive dark companion,  $M \gtrsim 2.3 M_{\odot}$  (Cowley et al. 1983), LMC X-3 became the first example of an extragalactic stellar-mass black hole.

LMC X-3 is an unusual system straddling the boundary between transient and wind-fed black hole binary systems (e.g., Soria et al. 2001). Its global characteristics, however, show that its mass transfer is governed by Roche-lobe overflow, which places it with the transients. Although it exhibits extreme X-ray variability, spanning roughly three orders of magnitude in luminosity, LMC X-3 is unique among the transients because, with a few notable exceptions (e.g. Smale & Boyd 2012; Wilms et al. 2001), it remains in a disk-dominated thermal state (approximately 90% of the time).

In fact, the dominance of the soft thermal component and the relative simplicity of LMC X-3's spectrum are the reasons Kubota et al. (2010) and Straub et al. (2011)

both chose the source to benchmark the performance of accretion-disk spectral models. Likewise, our group has used the extensive thermal-state data available for LMC X-3 to firmly establish the existence of a constant inner-disk radius in black hole binary systems (Steiner et al. 2010).

Recently, Smale & Boyd (2012) have identified two long-duration “low” phases, each lasting several months, during which the system was in a hard state. This unusual behavior is likely related to the well-known variability of the source on long timescales. Initially, Cowley et al. suggested a superorbital X-ray period of  $\sim 198$  (or possibly  $\sim 99$ ) days, but subsequent studies of both optical and X-ray variability find a range of superorbital periodicities extending from  $\sim 100 - 500$  days (Brocksopp et al. 2001; Wen et al. 2006; Kotze & Charles 2012). There is no stable long period in this source, and the superorbital variability appears not to be attributable to the precession of a warped disk or related at all to the orbital dynamics of the system. Instead, the long-term variability is likely produced by changes in the mass accretion rate (Brocksopp et al. 2001; hereafter B01).

Several groups have used the extensive data available for LMC X-3 to search for connections between X-ray variability and optical variability. Notably, B01 find that the X-ray and optical light curves are correlated, with an X-ray lag of 5–10 days, whereas Cowley et al. (1991) find a somewhat longer  $\sim 20$ -day lag.

A complementary body of work has focused on examining very fast ( $\lesssim 10$ s) variability in the hard state for other black-hole binary systems (e.g., Gandhi et al. 2010; Durant et al. 2011). In these systems, a surprising subsecond anticorrelation between X-ray and optical is

jsteiner@cfa.harvard.edu

<sup>1</sup> Harvard-Smithsonian Center for Astrophysics, 60 Garden Street, Cambridge, MA 02138.<sup>2</sup> Department of Astronomy, San Diego State University, 5500 Campanile Drive, San Diego, CA 92182-1221.<sup>3</sup> Astronomy Department, Yale University, P.O. Box 208101, New Haven, CT 06520-8101.<sup>4</sup> MIT Kavli Institute for Astrophysics and Space Research, MIT, 70 Vassar Street, Cambridge, MA 02139.<sup>5</sup> Department of Astronomy, Cambridge University, Madingley Road, Cambridge, CB3 0HA, UK.<sup>†</sup> Hubble Fellow.

commonly observed that is unlikely to be related to X-ray reprocessing. Rather, it appears that this behavior is related to the presence of a jet. In the case of LMC X-3, no jet is expected, particularly for the thermal state relevant here.

In the standard  $\alpha$ -disk theory of accretion (Shakura & Sunyaev 1973), one naturally expects the signals between any two wave bands to be correlated with a time delay that corresponds to the viscous time for a parcel of gas to travel from the outer emission region (longer wavelength band) in the disk to the inner (shorter wavelength band). Let us consider an annular region with an outer radius  $R$  and a gap in radius  $\Delta R$  between the two zones that are of interest in this paper, namely, the regions of optical and X-ray emission. Since the smaller radius in this case is negligible compared to  $R$ , the viscous time for gas with viscosity  $\nu$  to traverse the distance  $\Delta R \sim R$  is simply,

$$t_{\text{visc}} = R^2/\nu. \quad (1)$$

In this paper, we link the optical variability of LMC X-3 to its X-ray variability by using a wealth of optical and X-ray data. More specifically, we employ two extensive optical / infrared (OIR) data sets and, in the X-ray band, we combine data collected daily by *RXTE*'s All-Sky Monitor (ASM) with high-sensitivity data obtained in many hundreds of pointed observations using *RXTE*'s Proportional Counter Array (PCA).

## 2. DATA

Our principal OIR data set was obtained using the ANDICAM (Bloom et al. 2004) on the SMARTS 1.3 m telescope (Subasavage et al. 2010). ANDICAM is a dual-channel imager, which we used to obtain pairs of images of LMC X-3 in  $B$ ,  $V$ ,  $I$ , or  $J$ . The data were reduced and calibrated with respect to several field stars, as described in Orosz et al. (2014).

The ANDICAM data were supplemented by  $B$  and  $V$  data kindly supplied by C. Brocksopp and described in B01. These data are a subset from a larger sample obtained using the 0.91 m Dutch Telescope of the European Southern Observatory between 1993 and 1999 during a total of 16 different observing runs. Our full data set is derived from 470, 514, 476, and 440 SMARTS observations in  $B$ ,  $V$ ,  $I$ , and  $J$ , respectively, and 356 and 685 additional ESO observations in  $B$  and  $V$  (B01). We employ just  $\sim 75\%$  of the B01 data set, because we exclusively consider those data collected after 1996 March 7 (MJD  $\geq 50149$ ) when *RXTE* operations entered a mature phase.

Our *RXTE* X-ray data set is derived from both ASM and PCA observations. The calibrated ASM data using the full bandwidth (2–12 keV) and 1-day time bins were retrieved from the website supported by the ASM/*RXTE* team<sup>7</sup>. The PCA data, derived from 1598 observations made using the PCU-2 detector, were all reduced and analyzed following closely our standard methods (e.g., Steiner et al. 2010), but in this case the data were partitioned in somewhat finer time bins, using continuous exposure intervals with a mean of 2 ks (and range 300s to 5000s). Our goal here is relatively modest, namely, to

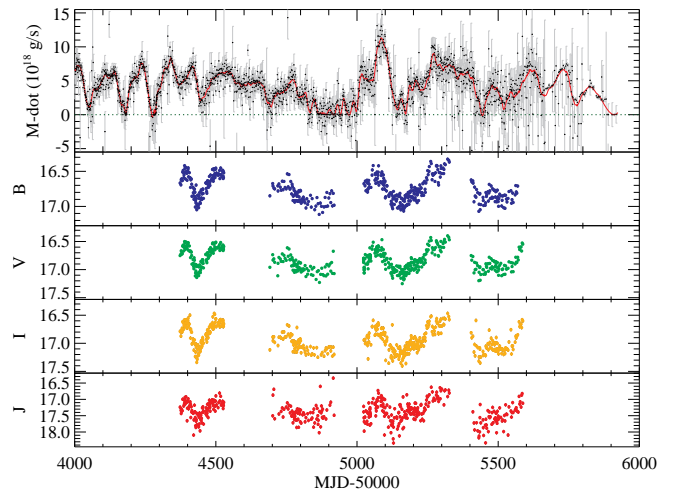


FIG. 1.— SMARTS OIR and *RXTE* X-ray (ASM + PCA) light curves. The light curve amplitude (top) is expressed in units of  $\dot{m}_X$ , as discussed in § 2.1. The red curve shows our adopted, smoothed light curve.

derive reliable estimates of flux and construct an X-ray light curve.

The SMARTS OIR light curves and the contemporaneous ASM + PCA X-ray light curve are shown in Figure 1.

### 2.1. Unifying PCA and ASM Data Sets

In order to most fully capture the X-ray variability of LMC X-3, we combine the ASM and PCA data sets into a single, unified light curve. Given the complementary cadence and sensitivity of the two instruments, this approach results in a light curve that for our purposes is distinctly superior to using only one of the light curves singly. The method we adopt here for combining the light curves does not critically affect our final results; e.g., the character of our results are unaffected if we use the ASM data alone.

We choose to standardize the two data sets by determining for each ASM and PCA observation the mass accretion rate onto the black hole,  $\dot{m}_X$ . We make this choice because LMC X-3 is nearly always in the thermal state, a state in which the stable inner-radius results in a constant efficiency (depending only on the spin parameter), and  $\dot{m}_X$  is therefore simply proportional to the bolometric luminosity emitted by the disk. The mass accretion rate determined from PCA spectral fits can be compared to the 2–12 keV PCA flux, providing a scaling relationship that is then used to determine  $\dot{m}_X$  values for the 2–12 keV flux measurements from ASM data, which cannot be fit for bolometric disk luminosity. Fortunately, when LMC X-3 does occasionally enter the hard state its luminosity is so low that  $\dot{m}_X \approx 0$  is a quite reasonable approximation for the purposes of this study.

We first determine  $\dot{m}_X$  for the PCA data by fitting the  $\sim 1600$  PCU-2 spectra to a standard disk model that accommodates the presence of a weak Compton component. The complete spectral model in *XSPEC* notation (Arnaud 1996) takes the form: TBABS\*(SIMPL\*KERRBB2). The disk component KERRBB2 (McClintock et al. 2006; Li et al. 2005) fits for  $\dot{m}_X$  using fixed – and here, approximate – values for black-hole mass, inclination and distance. SIMPL models the Compton power law (Steiner et al. 2009) and TBABS the

<sup>7</sup> [http://xte.mit.edu/ASM\\_lc.html](http://xte.mit.edu/ASM_lc.html)

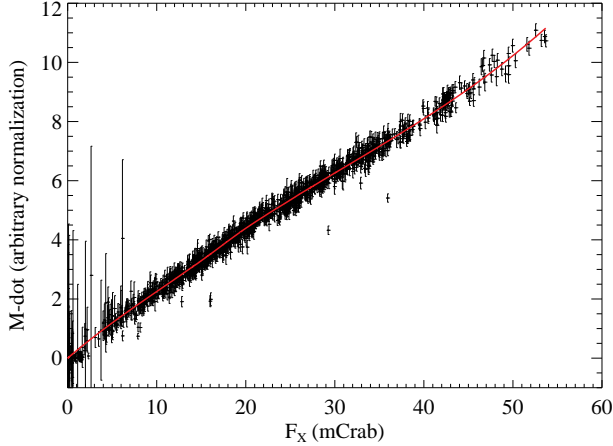


FIG. 2.— Spectral fitting results for the  $\sim 1600$  PCA spectra showing  $\dot{m}_X$  as a function of 2–12 keV X-ray flux. The LOWESS fit we adopt is overlaid in red. Results for 6% of the full PCA sample are omitted from the figure either because the spectral fit used to derive  $\dot{m}_X$  was statistically poor or it provided no constraint on  $\dot{m}_X$ .

low-energy absorption (Wilms et al. 2000). Each PCA spectrum thus delivers a value of the accretion rate<sup>8</sup> At the same time, we compute the *observed* PCA flux  $F_X$  from 2–12 keV relative to the standard flux of the Crab in the same band (Toor & Seward 1974). As illustrated in Figure 2, the relationship between  $\dot{m}_X$  and  $F_X$  obtained in this way is well defined and tightly constrained<sup>9</sup>.

We likewise converted the 2–12 keV ASM count rates into fluxes relative to the Crab (1 Crab = 75 ASM c s<sup>-1</sup>) and then interpolated the relationship derived for the PCA in order to establish the relation between flux and  $\dot{m}_X$  for the ASM. (To accommodate negative ASM count rates, we used an extrapolation of the low-flux PCA data rather than adopting a floor value for  $\dot{m}_X$ .)

Having established a common scale for the two detectors, we then used the LOWESS nonparametric smoothing algorithm (Cleveland 1979) to derive a representation of the true, underlying light curve (which is at all points locally determined). Because the errors are grossly different for the PCA and ASM data, we achieve appropriate weighting via Monte-Carlo randomization: A LOWESS curve fit is derived for each of 1000 random realizations and the median curve is taken as the most representative fit. Here, we used a third-order LOWESS curve fit and adopted a window length of approximately one month, a choice motivated by the X-ray autocorrelation time (§ 3). The precise settings used in fitting the data only affect our results cosmetically. For example, with a window length of 3 days, we obtained the same - though noisier - results.

### 3. CORRELATED VARIABILITY

<sup>8</sup> The other fit parameter of the disk component, spin, is allowed to vary, but is distributed with modest scatter about a fixed value. A separate paper is forthcoming on the spin of LMC X-3 (Steiner et al. 2014).

<sup>9</sup> Roughly 0.7% of the data, 11 data points, fall  $> 5\sigma$  below the curve. These exceptional spectra show an unusually strong Compton component, more than an order of magnitude brighter than is typical for the disk-dominated states of LMC X-3.

With the unified X-ray light curve now in hand (i.e.,  $\dot{m}_X(t)$ ), we use the unsmoothed data and examine the relationship between X-ray and OIR variability. Specifically, we assess the correlated variability between  $\dot{m}_X$  and the OIR bands as a function of time lag using the discrete correlation function (DCF) of Edelson & Krolik (1988), with all observation times referred to the Solar System barycenter. A DCF is derived from a pair of time series,  $A_i$  and  $B_j$ , by first establishing a set of lags  $\tau$  and cross-fluxes  $\Upsilon$ , which are calculated across all paired time differences amongst the data:

$$\Delta t_{ij} = t_i - t_j, \quad (2)$$

$$\Upsilon_{ij} = \frac{(A_i - \bar{A})(B_j - \bar{B})}{\sigma_A \sigma_B}, \quad (3)$$

where  $\bar{A}$  and  $\bar{B}$  are the means of series  $A$  and  $B$ , respectively. Similarly,  $\sigma_A$  and  $\sigma_B$  are the standard deviations of  $A$  and  $B$ . The DCF for time lag  $\tau$  is then

$$\text{DCF}(\tau) = \frac{1}{N(\tau)} \sum_{\Delta t_{ij} \in \tau} \Upsilon_{ij}, \quad (4)$$

where  $N(\tau)$  is the number of  $\Delta t_{ij}$  elements in the bin  $\tau$ .

We convert the OIR data into fluxes and then standardize all data sets to unity variance and zero mean and then compute a DCF between each OIR light curve and the (unsmoothed)  $\dot{m}_X$  time series (§ 2.1), binning the time lag data into  $\sim 1$  day intervals. Given this sampling and given data that span a decade, correlated variability is discernible over timescales ranging from days to years. As shown in Figure 3, the X-ray time lag for the strongest features in the cross correlation of  $\dot{m}_X$  with the OIR flux in each individual band is  $\approx 2$  weeks. This value is intermediate between those found by B01 and Cowley et al. (1991). A possible explanation for the differences is the lag's luminosity dependence discussed in § 6.

The lag of the X-ray flux is naturally explained as a consequence of the viscous time delay for a density perturbation to propagate from the outer disk, the location of peak OIR emission, to the vicinity of the black hole where the X-rays are produced.

Why are the cross-correlation peaks so broad? An examination of the X-ray autocorrelation (Figure 4) suggests an answer. The autocorrelation timescale over which the X-ray source brightens or dims, several weeks, is similar to the typical lag time of  $\approx 2$  weeks. This is not surprising given that the timescale for the inner disk to change from faint to bright - the autocorrelation time - should be commensurate with the time required for a parcel of gas to travel from the outer disk to the center, i.e., the viscous time.

On longer timescales, first at  $\sim 100$  days and 160 days, other features appear in the autocorrelation function (Figure 4). As evidenced by alternating positive/negative harmonic peaks, the anti-correlation feature at 160 days, e.g., is likely to be at least partially related to radiative or mechanical feedback in the system, whereby periods of strong accretion inhibit the accretion flow onto the outer disk. This is also evident in the strong anti-correlation signature between OIR and X-ray bands at  $\sim -120$  d lag (where the optical behavior now follows after the X-ray).

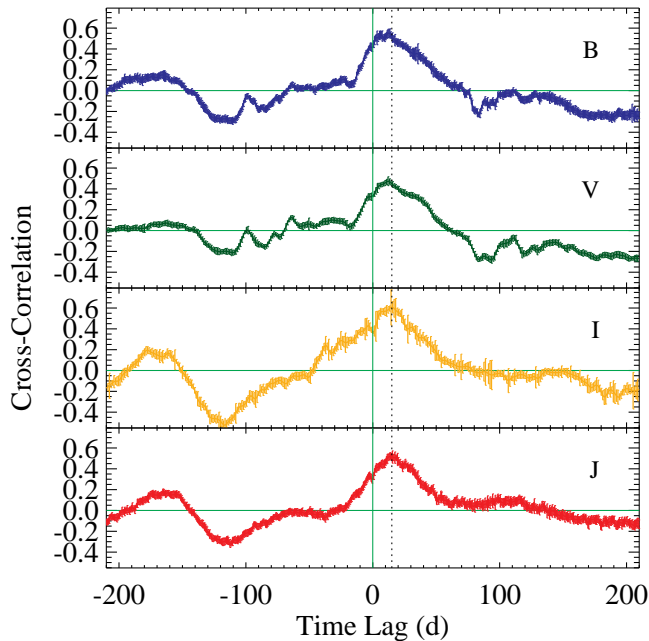


FIG. 3.— Cross-correlations between X-ray and four OIR bands. The vertical dotted line at 15 days is meant to guide the eye in assessing the  $\approx 2$  week X-ray lag. Random realizations have been used to assess the error for each cross-correlation, which is the source of scruff on the curves.

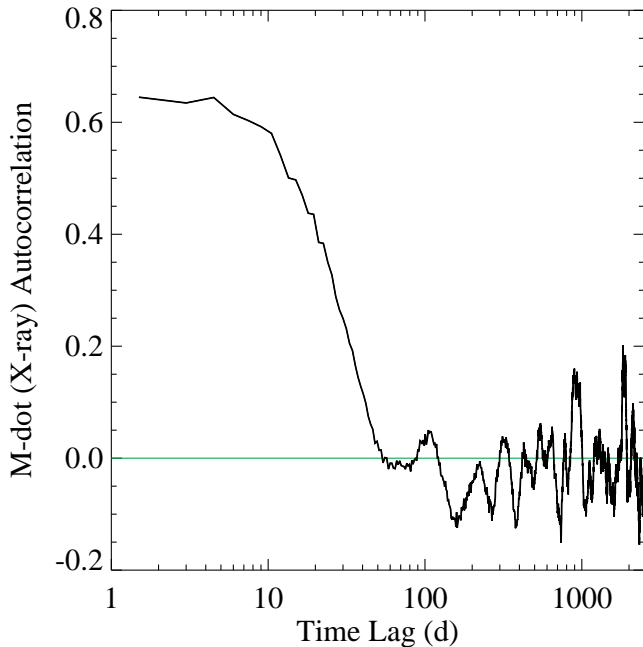


FIG. 4.— X-ray autocorrelation. The typical  $\approx 20$ -day “pulse-width” response of the X-ray light-curve shows that significant changes in the accretion flow require several weeks to materialize. This timescale is responsible for the breadth of the lag features in Fig. 3. Errors are shown but are generally comparable to or smaller than the linewidth.

In the next section, we develop a model for the accretion-driven,  $\approx 2$  week time lag in the context of a simplistic physical picture of the disk-star system in LMC X-3.

#### 4. THE ACCRETION MODEL

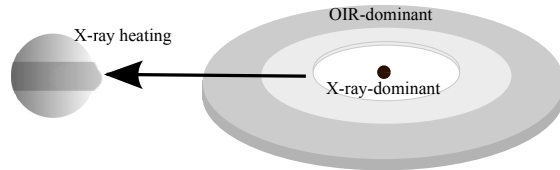


FIG. 5.— A schematic representation of our model for the binary system. The companion star on the left is shown heated by the central X-ray source at high latitudes and shielded by the disk in the equatorial region. The outer and inner regions of the disk (*not* to scale) produce respectively OIR and X-ray emission.

Our purpose is to model the complex OIR light curves of LMC X-3 as a blend of three components of emission attributable to (1) the companion star; (2) a multitemperature thermal disk; and (3) the regions in the disk and star where X-rays are reprocessed. (We need not consider synchrotron emission here, as there is no evidence for a jet in LMC X-3, unlike many other sources.) Our model for the system is shown schematically in Figure 5. We approximate the net emission  $F(t)$  in a given OIR band  $i$  as a sum of the three components:

$$F_i(t) = X_i(t) + S_i(t) + H_i(t), \quad (5)$$

where  $X_i(t)$  is the OIR disk emission which relates to the later X-ray emission (or  $\dot{m}_X$ ) at time  $t + t_{\text{visc}}$ ;  $S_i$  is the direct flux from the star plus any steady component of disk light; and  $H_i$  is the reprocessed emission from the outer disk and companion star.

##### 4.1. Stellar Component

The simplest term,  $S_i$ , is a constant plus sinusoidal terms that approximate the asymmetric ellipsoidal variability of the tidally distorted star:

$$S_i(t) \equiv C_i + c_i [\sin(4\pi\phi - \pi/2) + \epsilon e(\phi)], \quad (6)$$

where phase  $\phi \equiv (t - t_0)/P$  and

$$e(\phi) \equiv \max(0, \sin(4\pi\phi + \pi/2)) \times \begin{cases} 1, & \sin(2\pi\phi + \pi/4) > 0, \\ -1, & \sin(2\pi\phi + \pi/4) \leq 0 \end{cases} \quad (7)$$

allow for the difference in the amplitudes of the two minima. Both  $\epsilon$  and  $c_i$ , the normalizations respectively of the asymmetric and sinusoidal terms, are free parameters, as are  $t_0$ ,  $C_i$ , and  $P$ .

##### 4.2. Disk Component

The connection of the term  $X_i(t)$ , the variable OIR component of disk emission, to  $\dot{m}_X$  is obvious. However,  $\dot{m}_X$  was derived for the inner X-ray-emitting portion of the disk, which is located far from the optical-emitting region, and the mass transfer rates may be different in the two regions. Therefore, in order to compute the OIR disk emission from  $\dot{m}_X$ , our model must include a description of how matter flows from the outer disk to the inner region. This is established via a transfer function which maps between X-ray and OIR regimes. We envision the disk described with such a model as a series of concentric rings. The accretion flow for each individual ring is approximately steady-state, but the steady-state solution varies from ring to ring. The order of the rings are fixed, but they are allowed to stretch or compress in width during inflow.

Meanwhile, the observed, viscosity-induced time delay of the X-ray flux relative to the optical will have some dependence on the mass supply of the individual rings. In our generic prescription, we incorporate this dependence as a free power-law scaling on the time delay, which depends on  $\dot{m}_X$ , a choice that is explained further in Section 6. We likewise assume that the optical emission has a power-law dependence on  $\dot{m}_X$ :

$$X_i(t) \equiv a_i \times [\dot{m}_X(t + \delta t(t))/10^{18} g s^{-1}]^\beta, \quad (8)$$

with  $a_i$  and  $\beta$  as free parameters and  $\delta t(t)$  is the viscous lag at time  $t$ , defined as

$$\delta t(t) \equiv \Delta_i \left( \frac{\dot{m}_X(t + \delta t(t))}{\langle \dot{m}_X \rangle} \right)^\psi, \quad (9)$$

where  $\Delta_i$  and  $\psi$  are free parameters. A slightly modified prescription for the accretion emission is considered in Appendix B. Finally, we allow for a potential scaling error in our conversion from X-ray flux to  $\dot{m}_X$  by introducing a floating offset  $a_X$  which modifies the zero-point of  $\dot{m}_X$ . For simplicity, rather than introducing a new variable,  $\dot{m}_X$  will be understood to contain an implicit free zero-point, which is determined in the fit.

#### 4.3. Reprocessed Emission

The X-ray heating by the central source, which occurs on a timescale of seconds, is treated as instantaneous. That is, the heating term  $H_i(t)$  responds directly to changes in  $\dot{m}_X(t)$  (zero time lag). We arbitrarily parameterize the dependence of  $H_i(t)$  on  $\dot{m}_X$  as a broken power law. This choice allows for variable shielding by the disk as the X-ray luminosity varies.

The heating term contains two elements: The primary term, which has no orbital phase dependence, describes X-ray heating of the outer disk; and the secondary term,  $Z(t)$ , describes X-ray heating of the companion star.  $Z(t)$  depends on phase and is maximum at superior conjunction of the star. We assume that  $Z(t)$  varies sinusoidally and that its normalization constant  $h_i = h$  is the same for all of the OIR bands. This approximation is valid because for the B-type companion star (Cowley et al. 1983) the OIR bands all lie in the Rayleigh-Jeans part of the spectrum.

$$H_i(t) \equiv h c_i (1 + Z(t)) \begin{cases} (\dot{m}_X(t))^{\gamma_1}, & \dot{m}_X(t) < \dot{m}_{\text{break}} \\ \dot{m}_{\text{break}}^{\gamma_1} \left( \frac{\dot{m}_X(t)}{\dot{m}_{\text{break}}} \right)^{\gamma_2}, & \dot{m}_X(t) > \dot{m}_{\text{break}} \end{cases} \quad (10)$$

where

$$Z(t) = \eta/2 (1 + \sin(2\pi\phi - \pi/2)), \quad (11)$$

so that  $Z(t)$  varies between 0 and  $\eta$  each orbit, where  $\eta$ ,  $h$ ,  $\gamma_1$ ,  $\gamma_2$ , and  $\dot{m}_{\text{break}}$  are fit parameters.

Our full model consists of a total of 27 free parameters (plus two additional calibration parameters to align the B01 and SMARTS datasets). There are 16 “chromatic” parameters that contain a subscript  $i$  (4 each per OIR band) and there are 11 “gray” parameters that are independent of wavelength (e.g., the orbital period  $P$ ). Correlations amongst the fit parameters are discussed and shown in Appendix A.

## 5. RESULTS

The model has been implemented in *python* and applied at once to the composite OIR data set. All fits are computed using the Markov Chain Monte-Carlo (MCMC) routine *emcee-hammer* (Foreman-Mackey et al. 2013) in a Bayesian formalism. Because our model is an oversimplification of complex real processes, we expect the quality of the fits to be limited by systematic effects. We therefore adopt 10% and 20% (systematic) error bars for the optical and IR data, respectively, and we ignore the much smaller measurement errors. These round values were chosen by making a preliminary fit to the data and assessing the rms fit residuals. Because the uncertainties were estimated in this utilitarian way, any goodness-of-fit statistics -such as  $\chi^2/\nu$ - should be interpreted with reserve.

We use a flat prior (i.e., uniform weighting) on the period; for all other parameters, we use informed priors whenever one is evident. Otherwise, we default to flat priors on the logarithm of normalization terms (i.e., scale-independent weighting), and flat priors on shape parameters. The fitting results, which are based on our analysis of all the OIR data, are presented in Table 1. MCMC directly computes the posterior probability distribution of a model’s parameters, but it does not specifically optimize the fit quality. Therefore, the best-fitting value of  $\chi^2/\nu$  given in Table 1 has been obtained via other standard optimization methods (e.g., Levenberg-Marquardt, downhill-simplex, etc.), while taking the MCMC results as a starting point.

To achieve our fits via *emcee-hammer*, we used 500 walkers with 15000 steps apiece for a total of 7.5 million MCMC samples. Our analysis and results are based on the final 2.5 million samples. Convergence has been diagnosed following Gelman & Rubin (1992) using a stringent criterion of  $\tilde{R} < 1.1$ . For our analysis, across all parameters,  $1.049 < \tilde{R} < 1.085$ .

In Figure 6, we show for the V-band light curve (the band with the most data) the best-fit model broken down into its component contributions. The figure makes clear that the total flux is dominated by the constant component of stellar light, while the disk and X-ray-heating component contributions are at most  $\sim 1/2$  and  $\sim 1/4$  as large, respectively (as determined in the fit). The *maximum* contribution of X-ray heating to the total stellar flux is  $h\dot{m}_{\text{break}}^{\gamma_1} \sim 0.16\%$ . Meanwhile, the contribution to the stellar flux due to ellipsoidal variability is  $c_i/C_i \approx 5 - 10\%$  (Section 4.1), while the asymmetric term is a factor  $\sim 10$  smaller still. B01 conclude that the optical variability of LMC X-3 is due to viscous disk emission rather than X-ray reprocessing, i.e., that reprocessing is of secondary importance. Our results support B01’s conclusion.

Our fits indicate that as the X-ray flux varies over its full range that the fraction of stellar light to the total light in both the  $B$  and  $V$  bands is  $\sim 80\% \pm 10\%$ . A consistent value of  $\approx 70\% - 90\%$  has been derived independently for a wide range of X-ray luminosities using spectroscopic data (Orosz et al. 2014).

The value of the scaling index  $\beta = 1.31 \pm 0.08$  (90% confidence), which relates the OIR flux to the time-lagged disk emission  $\dot{m}_X$  (Section 4.2), may indicate



that the rates of inflow at the outer and inner radii are not matched. If so, the implication is that mass is lost from the body of the disk, especially at high values of  $\dot{m}_X$ . This scenario is readily explained by the action of disk winds (e.g., Miller et al. 2006; Luketic et al. 2010; Ponti et al. 2012; Neilsen & Homan 2012). Alternatively, as discussed in § 6, a standing shock from the accretion stream could be responsible for the mismatch in rates.

From the flux densities computed in Table 1, very rough constraints can be placed on the temperature of the star and of the OIR-emitting region of the disk. However, such calculations are fundamentally limited by the accuracy of the absolute OIR flux calibration, which is marred by 20–30% zero-point calibration differences between SMARTS and B01 data sets. We rely on the SMARTS calibration as our standard rather than that of B01 because the former calibration is based on a larger sample of standard stars that were observed more frequently.

In Figure 7, we show two versions of the OIR light curves folded on LMC X-3’s orbital period: On the left are the light curves in their original form, and on the right are the filtered light curves produced by removing the two nonstellar contributions, i.e., the  $\dot{m}_X$ -induced component  $X(t)$  and the reprocessed X-ray emission  $H(t)$ . Plainly, the ellipsoidal variability is much more apparent in the filtered light curves.

Because of the long baseline and abundance of data, the signal evident from the filtered light curves (using the complete model) allows one to determine the 1.7-day orbital period to the remarkable precision of two-tenths of a second. (Prior to this work, the best determination of the period has been  $P = 1.7048089 \pm 1.1 \times 10^{-6}$  d (Song et al. 2010); our result is in good accordance with theirs.) The orbital phase, however, conforms to its prior and is otherwise unconstrained. The quality of our period determination is illustrated in Figure 8 where it is shown to compare favorably with an independent determination based on three decades of spectroscopic velocity data. As indicated in the figure, the two data sets jointly determine the period to a precision of 90 milliseconds ( $P = 1.704808 \pm 1 \times 10^{-6}$  d).

The raw light curves, by comparison, cannot even deliver a unique orbital period because of strong aliasing. A Lomb-Scargle (Scargle 1982) search shows that the strongest false period is favored 9:1 over the true period. Moreover, the uncertainty in the period determination is a factor  $\sim 3$  worse than achieved using the light curve model.

## 6. DISCUSSION

### 6.1. Reprocessing and Self-Shadowing

The intensity of the X-ray heating component in the OIR bands is a surprisingly strong function of X-ray luminosity, scaling as  $H_i \propto \dot{m}_X^{1.9}$ , up to a critical value of  $\dot{m}_X \approx 6.2 \times 10^{18}$  g/s (roughly  $\sim 50\%$  of the Eddington limit). Above this luminosity, the heating signal drops off rapidly as  $\dot{m}_X^{-3.4}$  such that at the maximum X-ray luminosity ( $\approx L_{\text{Edd}}$ ) its intensity is a factor of 10 below its peak. A likely explanation for the initial superlinear rise with luminosity is that the flaring of the disk at higher luminosity increases the solid angle of the re-

processing region, and that this effect dominates over the self-shadowing by the disk. Above  $\sim 50\%L_{\text{Edd}}$ , the shadowing dominates and the heating signal dwindles rapidly.

For the shadowing to be substantial without producing more OIR emission than is observed, the flare in the disk’s scale height must move inward as the X-ray luminosity increases. That is, we envision a flared funnel-like region in the inner disk that contracts in around the black hole as luminosity increases and as the flaring becomes more pronounced. The OIR emission from the reprocessing region remains modest, even at the highest luminosities, because the reprocessing excess is relegated to shorter wavelengths and emitted from within a diminished area of the disk. A prediction of this picture is that the pattern of reprocessing shifting to smaller area and shorter wavelength at growing luminosity should be observable in optical / UV for those low-inclination systems which show substantial luminosity variability.

As viewed from the X-ray source, the star subtends an angle of  $\sim 37^\circ$  (ignoring disk obscuration). The corresponding fraction of the X-ray heating signal that is reprocessed in the face of the star is obtained from the fit:  $\eta/(1+\eta) \approx 40\%$  (Equations 10,11). The reprocessed emission from the star can be distinguished from the reprocessed disk emission because the former is modulated at the orbital period. For simplicity, the fraction of the total reprocessed emission contributed by the star is treated as a constant, free parameter.

### 6.2. Wavelength-Independence of the Lag

In canonical thin accretion disk theory (Shakura & Sunyaev 1973), the wavelength of peak emission from the disk scales as  $\lambda_{\text{max}}(R) \propto R^{3/4}$ , whereas for irradiation-dominated disks the peak wavelength scales roughly as  $\lambda_{\text{max}}(R) \propto R^{3/7}$  (Chiang & Goldreich 1997). On this basis, one expects a factor  $\sim 2$  variation in the viscous time lag across the OIR bands. However, as evident from Table 1 and from inspection of Fig. 3, the OIR time lag is essentially independent of wavelength from the *B*-band ( $\approx 4400$  Å) to the *J*-band ( $\approx 12,500$  Å)<sup>10</sup>.

The constancy of the viscous time lag with wavelength implies that the OIR signal arises from a single radius in the disk. This result is incompatible with any simple disk theory for which temperature falls off monotonically with radius, unless one imagines locating the radius of OIR emission at the disk’s outer edge. However, the outer edge is obviously ruled by the data because the entire disk would then be so hot that it would outshine the star.

### 6.3. Shocks and Hotspots in the Outer Disk

Instead, the constancy of the time lag with wavelength is naturally explained by the presence of a “hot spot” or similar structure within the outer disk that is bright enough to dominate the OIR lag signal. Doppler modulation tomographic maps of accreting binary systems show clear evidence for such features in other sources (e.g., Steeghs 2004; Calvelo et al. 2009; Kupfer et al. 2013). An excellent example is provided by the map of the black hole binary A0620-00, which reveals bright spots embedded in a hot “ring” in the disk (dominated by two

<sup>10</sup> The wavelength-independence of the lag has been verified by examining sub-intervals of the data as well.

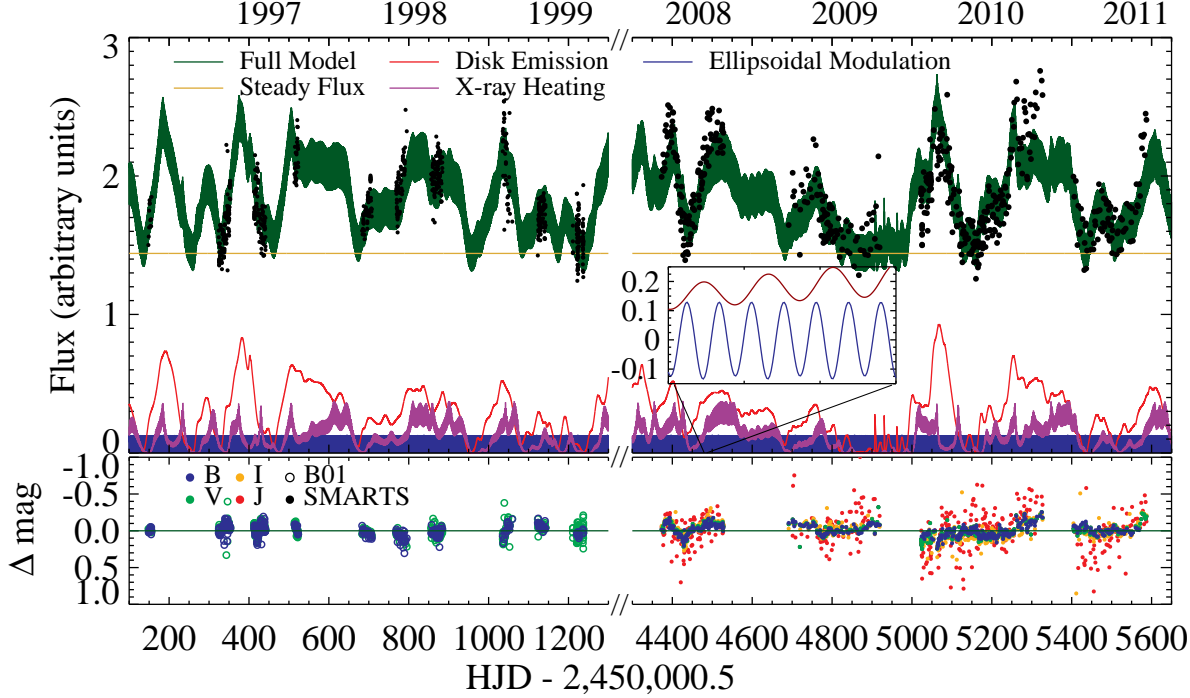


FIG. 6.— The model of the observed light curve and its three components for the band with the most data,  $V$ . The composite model is shown in dark green; the accretion emission derived using the X-ray data in red; and the ellipsoidal and X-ray-heating components are shown in blue and purple, respectively. The inset is a blowup showing the ellipsoidal and X-ray heating terms for several orbital cycles. The fit residuals are shown in the lower panels.

large crescent structures; Neilsen et al. 2008). The ring is located at 45% or 60% of the  $L1$  radius ( $R_{L1}$ ) depending on whether one assumes, respectively, a Keplerian or ballistic trajectory for the gas stream. This range in radius exactly brackets the *circularization radius* of the system, the radius at which the angular momentum of the tidal stream matches the angular momentum of the gas in the disk. The circularization radius  $R_C$  is located at 50%  $R_{L1}$  for A0620-00, while the truncation radius of the outer disk is predicted to be located at  $\sim 80 - 90\%$   $R_{L1}$  (Frank et al. 2002). A schematic diagram of a system like A0620-00 is shown in Figure 9.

The temperatures of these bright spots and rings are poorly constrained in quiescent black-hole binaries, and they are essentially unconstrained in active systems. In order to crudely gauge the temperature of such a spot, we look to the recent work by Kupfer et al. (2013) where for a cataclysmic variable (CV) system they have measured  $T_{\text{hotspot}} \approx 30,000$  K. Such hot spots are attributed to shocks produced by the tidal stream of gas from the companion star impinging on the disk. A strong shock (Mach number  $\mathcal{M} > 10$ ) can result in up to a hundred-fold jump in temperature in the post-shock gas.

If the mass flow rate in the stream  $\dot{m}_s$  is sufficiently large, a shock that traverses inward from  $R_{\text{out}}$  will eventually stall at the circularization radius  $R_C$ . For simplicity, we assume that the flow is purely ballistic, i.e., that the velocity is unaffected by  $\dot{m}_s$ , and that the hotspot luminosity increases as  $\dot{m}_s$  increases. We now mention

an alternative explanation for the superlinear scaling between OIR and X-ray emission ( $\beta = 1.3$ ), which in Section 5 we attributed to disk winds. Here, where the OIR emission originates in a shock, we instead envision that this nonlinear relationship could plausibly result from changes in the structure or strength of the shock caused by variations in  $\dot{m}_s$ .

#### 6.4. Estimating $\alpha$ -viscosity

The cooling time for the shock-heated gas is negligibly short compared to the viscous timescale. Therefore, the stability and brightness of these structures are related to the instantaneous value of  $\dot{m}_s$ . The ring itself must be relatively narrow owing to the prompt cooling. The cooled gas relaxes to the disk profile, and then it proceeds inward to the center on the viscous timescale.

The outermost disk is always dominated by gas pressure so that the scale height at each radius is given, roughly, by the ratio of the sound speed in the mid-plane,  $c_s = \sqrt{kT/\mu m_p}$ , to the Keplerian velocity in the disk. Using the  $\alpha$  disk approximation for disk viscosity (Shakura & Sunyaev 1973),

$$\nu = \alpha c_s z, \quad (12)$$

where  $z$  is the scale height of the disk. Then,

$$\nu \equiv \alpha c_s^2 \frac{R^{3/2}}{\sqrt{GM}}, \quad (13)$$

TABLE 1  
BEST-FITTING MODEL

Param.	Global	B	V	I	J	Prior <sup>a</sup>
$P$ (d)	$1.704805 \pm 3 \times 10^{-6}$	...	...	...	...	Flat
$\beta$	$1.31 \pm 0.08$	...	...	...	...	$N(1, 0.5)$
$\dot{m}_{\text{break}}/\max(\dot{m}_X)$	$0.545^{+0.017}_{-0.006}$	...	...	...	...	Log
$\psi$	$0.24^{+0.03}_{-0.04}$	...	...	...	...	Flat
$a_X (10^{18} \text{ g s}^{-1})$	$0.08^{+0.11}_{-0.03}$	...	...	...	...	Flat
$t_0 - T_{0,\text{Cowley}}^b$ (d)	$0.004^{+0.012}_{-0.017}$	...	...	...	...	$N(0, 0.01)$
$\Delta_i$ (d)	...	$15.5 \pm 1.1$	$15.4 \pm 0.8$	$16.4 \pm 1.1$	$16.3^{+1.1}_{-0.3}$	Flat
$a_i (\mu\text{Jy})$	...	$17 \pm 3$	$15 \pm 3$	$9.4^{+2.1}_{-1.6}$	$5.0^{+1.3}_{-0.8}$	Log
$c_i (\mu\text{Jy})$	...	$62 \pm 6$	$46 \pm 4$	$22 \pm 4$	$9^{+5}_{-3}$	Log
$C_i (\mu\text{Jy})$	...	$670 \pm 11$	$547 \pm 8$	$285 \pm 6$	$146 \pm 4$	Log
$\Delta m_B^c$	$0.293 \pm 0.012$	...	...	...	...	Flat
$\Delta m_V^c$	$0.216^{+0.008}_{-0.012}$	...	...	...	...	Flat
$\log_{10}(h)$	$-2.3^{+0.2}_{-0.3}$	...	...	...	...	Log on $h$
$\gamma_1$	$1.9 \pm 0.3$	...	...	...	...	$N(1, 0.5)$
$\gamma_2$	$-3.4^{+0.7}_{-1.0}$	...	...	...	...	Flat
$\eta$	$0.7^{+0.3}_{-0.2}$	...	...	...	...	Flat
$\log_{10}(\epsilon)$	$-1.1^{+0.4}_{-0.6}$	...	...	...	...	Flat on $\epsilon$
$\chi^2/\nu^d$	2426 / 2894					

NOTE. — Best fit model and associated 90% credible intervals. Of the 29 parameters, 16 are normalization terms to the component fluxes.

<sup>a</sup> The shape of the prior assumed. “Flat” indicates uniform weighting, and “log” refers to uniform weighting on the logarithm of the parameter.  $N(\mu, \sigma)$  describes a Gaussian centered upon  $\mu$  with standard deviation  $\sigma$ .

<sup>b</sup>  $T_{0,\text{Cowley}} = 2445278.66$  HJD (Cowley et al. 1983).

<sup>c</sup> Zero-point differences between the datasets of B01 and SMARTS.

<sup>d</sup> The goodness-of-fit is calculated using 10% systematic uncertainty on the optical model and 20% systematic uncertainties on the IR; the small measurement errors on the data contribute negligibly and were ignored.

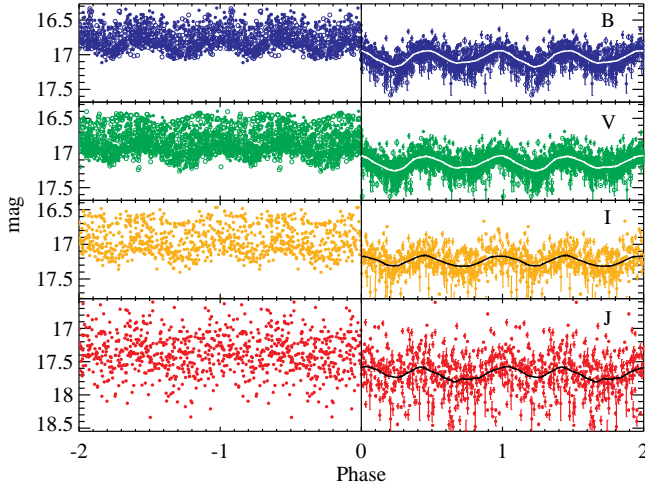


FIG. 7.— (left) OIR light curves folded on the orbital period. A zero-point offset has been applied to bring the B01 data (open symbols) into alignment with the SMARTS data (filled symbols). The shift is roughly 0.3 and 0.2 mag in  $B$  and  $V$  respectively (see Table 1). (right) OIR light curves obtained after removing the heating and disk-emission terms  $H(t)$  and  $X(t)$ . Error bars reflect an estimated 20% uncertainty on the accretion “noise” which has been subtracted. A LOWESS smoothing of the light curve is overlaid on the data in each panel to guide the eye.

and the viscous timescale can be written as

$$t_{\text{visc}} \approx \sqrt{GMR} \left( \frac{\mu m_p}{\alpha k T} \right). \quad (14)$$

In what follows, recall that we are approximating the evolving disk as a superposition of independent, steady-state solutions (Section 4.2). We make two other assumptions, which are eminently reasonable: (1) The disk

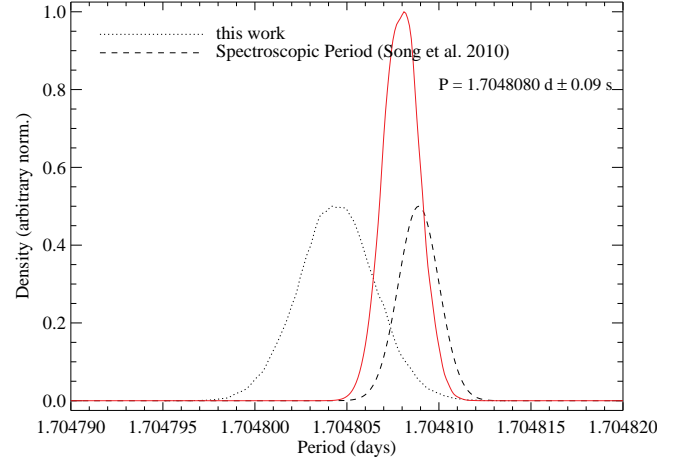


FIG. 8.— Our result for the orbital period alongside the definitive spectroscopic determination (Song et al. 2010). The combined result is shown in red.

is strongly illuminated; and (2)  $\dot{m}_s$  alone determines the X-ray and OIR emission. Building on these assumptions and our measured value of the time lag, we now derive a rough estimate of  $\alpha$  in the outer disk. We first consider the conditions in the disk and the location of the OIR-emitting hotspots.

The strong X-ray irradiation of the disk will modify its structure at large distances from the central source, i.e.,  $R > 10^{10}$  cm (Hartmann 1998). Meanwhile, the midplane temperature, being less sensitive to irradiation, will tend to follow the viscous dissipation profile,  $T_m \propto R^{-3/4}$ . However, the temperature of the irradiated surface layer of the disk will fall off much more slowly,



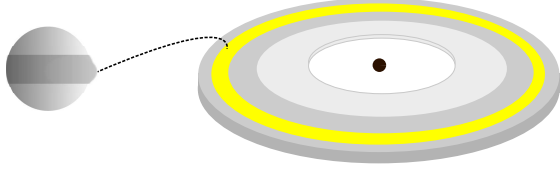


FIG. 9.— The OIR lag signal is dominated by a bright ring (yellow) in the outer disk at which the accretion stream (dashed line) shocks into the disk. This ring may coincide with the circularization radius, where the angular momentum of the accretion stream (dashed line) matches the disk’s Keplerian angular momentum.

as  $T_s \propto R^{-3/7}$  (Chiang & Goldreich 1997), or even as slowly as  $T_s \propto R^{-1/3}$  (Fukue 1992). To our knowledge, the vertical temperature gradient in strongly irradiated disks has not been given serious consideration. Generally,  $T_s$  and  $T_m$  in the outer disk, determined from irradiation and viscous dissipation, respectively, are comparable and within a factor of a few of one another, and it is reasonable to approximate the vertical temperature profile as isothermal (e.g., Cunningham 1976; King 1998). For the average mass accretion rate onto LMC X-3, we estimate for any reasonable set of disk parameters that to within a factor  $\sim 3$  the midplane temperature  $T_C \sim 10^5$  K at  $R_C$ .

For this temperature and radius, using Equations 12-14 we find to order of magnitude that  $\alpha \sim 0.5$ . Our result agrees well with other measurements of  $\alpha$ , particularly those obtained for CVs (King et al. 2007, and references therein). The most reliable of these other measurements, like our estimate for LMC X-3, were derived for irradiated outer disks.

### 6.5. $\alpha$ Scales with Luminosity

A surprising outcome of our model and analysis is the positive luminosity scaling of the time lag ( $\psi \approx 0.25$ ; Eq. 9). Recalling that  $t_{\text{visc}} \propto \dot{m}_X^\psi$ , Eq. 14 gives  $\alpha t_{\text{visc}} \propto T^{-1} \propto \dot{m}_X^{-1/4}$ . For a constant value of  $\alpha$ , one expects to find  $\beta = -0.25$ , whereas we find a positive value of  $\beta$ . As a bottom line, we find that the viscosity parameter varies with luminosity (or equivalently, mass accretion rate) as  $\alpha \propto \dot{m}_X^{-1/2}$ . An inverse scaling such as we predict has in fact, already been suggested for LMC X-3 based purely on changes in its disk spectra as the luminosity varies (Straub et al. 2011).

If this scaling is related to the increase in temperature which results from a higher  $\dot{m}_X$ , then  $\alpha$  may be lower in the inner disk<sup>11</sup>. However, GRMHD simulations indicate that  $\alpha$  increases as radius decreases, at least for the innermost disk where MHD turbulence is dominant (Penna et al. 2013). Of course, there is no reason to expect viscosity to be constant over the disk. In particular, the viscosity may depend on other factors such as the disk’s density, temperature or magnetization.

Bai & Stone (2011) provide one possible explanation for the scaling relation we find relating  $\alpha$  and luminosity. These authors find an inverse scaling between  $\alpha$  and

the ratio of gas-to-magnetic pressures,  $P_{\text{gas}}/P_{\text{mag}}$  (a net quantity usually referred to as “plasma  $\beta$ ”). Given the scaling,  $\alpha \propto P_{\text{mag}}/P_{\text{gas}}$ , if  $P_{\text{mag}}$  is sufficiently insensitive to the accretion flow in the outer disk, then one would expect that as the mass transfer rate ( $\dot{m}$ ) varies, when  $\dot{m}$  increases,  $P_{\text{gas}}$  will too. A more specific prediction would be beyond scope of this work, but we note qualitatively that this effect very naturally gives rise to an inverse relationship between  $\alpha$  and mass accretion rate, as required by our fit.

## 7. CONCLUSIONS

Motivated by a roughly two-week time-lagged correlation between the OIR and X-ray light curves of LMC X-3, we develop a new method of analysis that is applicable to active X-ray binary systems. We model the OIR emission deterministically as a combination of accretion emission, X-ray reprocessing, and stellar emission. The components driven by accretion are computed using the X-ray light curve. The model allows accretion signals to be filtered out of the OIR light curves, thereby isolating the stellar component of light.

The utility of this technique is demonstrated for LMC X-3, a system which exhibits large-amplitude, but simple, variability in its perennial thermal state. We demonstrate that this method improves the observability of the stellar ellipsoidal light curves and leads to an improved determination of the orbital period. Furthermore, the method allows one to disentangle the OIR component of disk emission from the reprocessed X-ray emission. The time lags in the system are independent of wavelength, which indicates that they originate from a hot ring at a single, fixed radius in the disk. We identify the radius of this ring as the circularization radius where the tidal stream from LMC X-3’s B-star companion meets the disk, inducing a bright shock.

By interpreting our results through the lens of  $\alpha$ -disk models, we estimate the viscosity in the outer disk: Based upon the average properties of the disk, we estimate  $\alpha \sim 0.5$  to order magnitude. Furthermore, we unexpectedly find that  $\alpha$  diminishes as luminosity increases ( $\alpha \propto \dot{m}_X^{-1/2}$ ). We speculate that this result may be related to changes in  $P_{\text{gas}}/P_{\text{mag}}$  related to evolution in the mass accretion rate in the outer disk (e.g, Bai & Stone 2011).

It is a pleasure to thank Poshak Gandhi, Chris Done, Ramesh Narayan, Andy Fabian, and Joey Neilsen for helpful discussions which have improved this work, as well as the anonymous referee, for her/his helpful review. We thank Catherine Brocksopp for making her B01 data set available to us, and Xuening Bai for his input on disk theory. Support for JFS has been provided by NASA Hubble Fellowship grant HST-HF-51315.01.

<sup>11</sup> On the other hand, this dependence cannot be *purely* due to an inherent scaling with temperature, i.e.  $\alpha \propto T^{-2}$ , without

the  $\alpha$ -disk interpretation breaking down. A weaker scaling with temperature would be compatible.

TABLE 2  
BEST FIT WITH MODEL 2

Param.	Global	B	V	I	J	Prior
$P$ (d)	$1.704805 \pm 3 \times 10^{-6}$	...	...	...	...	Flat
$\beta$	$1.29 \pm 0.08$	...	...	...	...	$N(1, 0.5)$
$\dot{m}_{\text{break}}/\max(\dot{m}_X)$	$0.546^{+0.012}_{-0.006}$	...	...	...	...	Log
$\log_{10}(a_2)$	$0.1^{+0.2}_{-0.3}$	...	...	...	...	Flat on $a_2$
$a_3$	$0.4 \pm 0.4$	...	...	...	...	Flat
$\psi$	$0.31^{+0.04}_{-0.05}$	...	...	...	...	Flat
$a_X(10^{18} \text{ g s}^{-1})$	$0.10 \pm 0.09$	...	...	...	...	Flat
$t_0 - T_{0,\text{Cowley}}$ (d)	$0.001 \pm 0.014$	...	...	...	...	$N(0, 0.01)$
$\Delta_i$ (d)	...	$12.6 \pm 1.0$	$12.6 \pm 0.8$	$15.4 \pm 1.2$	$11.2 \pm 1.5$	Flat
$a_i(\mu\text{Jy})$	...	$17^{+4}_{-3}$	$16 \pm 3$	$9.9 \pm 1.9$	$5.2 \pm 1.1$	Log
$c_i(\mu\text{Jy})$	...	$61 \pm 6$	$47 \pm 4$	$22 \pm 4$	$10 \pm 4$	Log
$C_i(\mu\text{Jy})$	...	$677 \pm 10$	$551^{+6}_{-9}$	$287 \pm 6$	$148 \pm 4$	Log
$\Delta m_B$	$0.293 \pm 0.012$	...	...	...	...	Flat
$\Delta m_V$	$0.215 \pm 0.010$	...	...	...	...	Flat
$\log_{10}(h)$	$-2.6^{+0.3}_{-0.4}$	...	...	...	...	Log on $h$
$\gamma_1$	$2.3 \pm 0.4$	...	...	...	...	$N(1, 0.5)$
$\gamma_2$	$-3.5 \pm 0.9$	...	...	...	...	Flat
$\eta$	$0.8 \pm 0.3$	...	...	...	...	Flat
$\log_{10}(\epsilon)$	$-1.1^{+0.3}_{-0.7}$	...	...	...	...	Flat on $\epsilon$
$\chi^2/\nu$	2395 / 2892					

NOTE. — Best fit model and associated 90% credible intervals. All notes from Table 1 are also applicable here.

## APPENDIX

### CORRELATIONS WITHIN THE FIT

Our model has many free parameters ( $\approx 30$ ), and it is therefore nontrivial to assess parameter degeneracies in the model. In Figure 10 we present pairwise correlations from a randomly-selected subsample of the MCMC chains for the principal fit parameters of the model. Parameters which are independently determined for the various OIR bands are shown together in color.

Few trends are strongly evident. The strongest is an anticorrelation between  $\gamma_1$ , the index which relates the degree of X-ray heating to luminosity, and the normalization to that scaling,  $h$  (Eq. 10). Also evident is a much weaker and positive correlation between  $\gamma_2$  and  $h$ .

Next-most prominent is an anticorrelation between  $\beta$  and the disk emission strength  $a_i$ , where the effect is strongest for shorter wavelengths. While the wavelength dependence of a given pair of model parameters does not necessarily indicate a degeneracy in the model, it can nevertheless be revealing. In particular, strongly positive trends with wavelength are evident and expected amongst parameters that characterize the disk brightness and stellar brightness (i.e., panels with pairs of  $a_i$ ,  $c_i$ , and  $C_i$ ). Conversely, the *wavelength independence* of the accretion lag,  $\Delta_i$ , an important result from this work, is evident in Figure 10.

### CONSIDERING NON-STATIONARY BEHAVIOR

One drawback to our approach is that although we model dynamic evolution of the accretion-disk system, we have adopted a structure rooted in a steady-state formalism. We now consider an improved treatment of non-stationary behavior with our model. Descriptively, we better allow for compression and expansion of the individual annuli by introducing a term that allows for stretching action by adjacent rings. Specifically, we modify Equation 8 by allowing X-ray heating to depend on the time derivative of the inner-disk accretion rate,  $\dot{m}_X$ . With this modification, Equation 8 becomes

$$X_i(t) \equiv a_i \times \left[ \frac{\dot{m}_X(t + \delta t(t))}{10^{18} \text{ g s}^{-1}} + a_2 \frac{\dot{m}_X(t + \delta t(t))}{10^{18} \text{ g s}^{-2}} \times \left( \frac{\dot{m}_X(t + \delta t(t))}{10^{18} \text{ g s}^{-1}} \right)^{a_3} \right]^\beta, \quad (\text{B1})$$

where  $a_2$  and  $a_3$  are additional free parameters used to determine radial expansion or compression of the flow. This alternate formulation has only a minor affect on the fits to the OIR light curves; the fitting results are given in Table 2. The quality of the fit is only moderately improved,  $\Delta\chi^2 = 29$  for two additional free parameters. The principal change is that the (average) time lag inferred is smaller by  $\approx 20\%$  compared to the principal model, which is perhaps a consequence of a phase shift induced when mixing the  $\dot{m}_X$ -light curve with its time derivative. Detailed consideration of non-stationary disk modeling within the paradigm of a bifurcated, two-state accretion flow, as applied to LMC X-3, can be found in Cambier & Smith (2013).

## REFERENCES

- Arnaud, K. A. 1996, in *Astronomical Society of the Pacific Conference Series*, Vol. 101, *Astronomical Data Analysis Software and Systems V*, ed. G. H. Jacoby & J. Barnes, 17
- Bai, X.-N., & Stone, J. M. 2011, *ApJ*, 736, 144

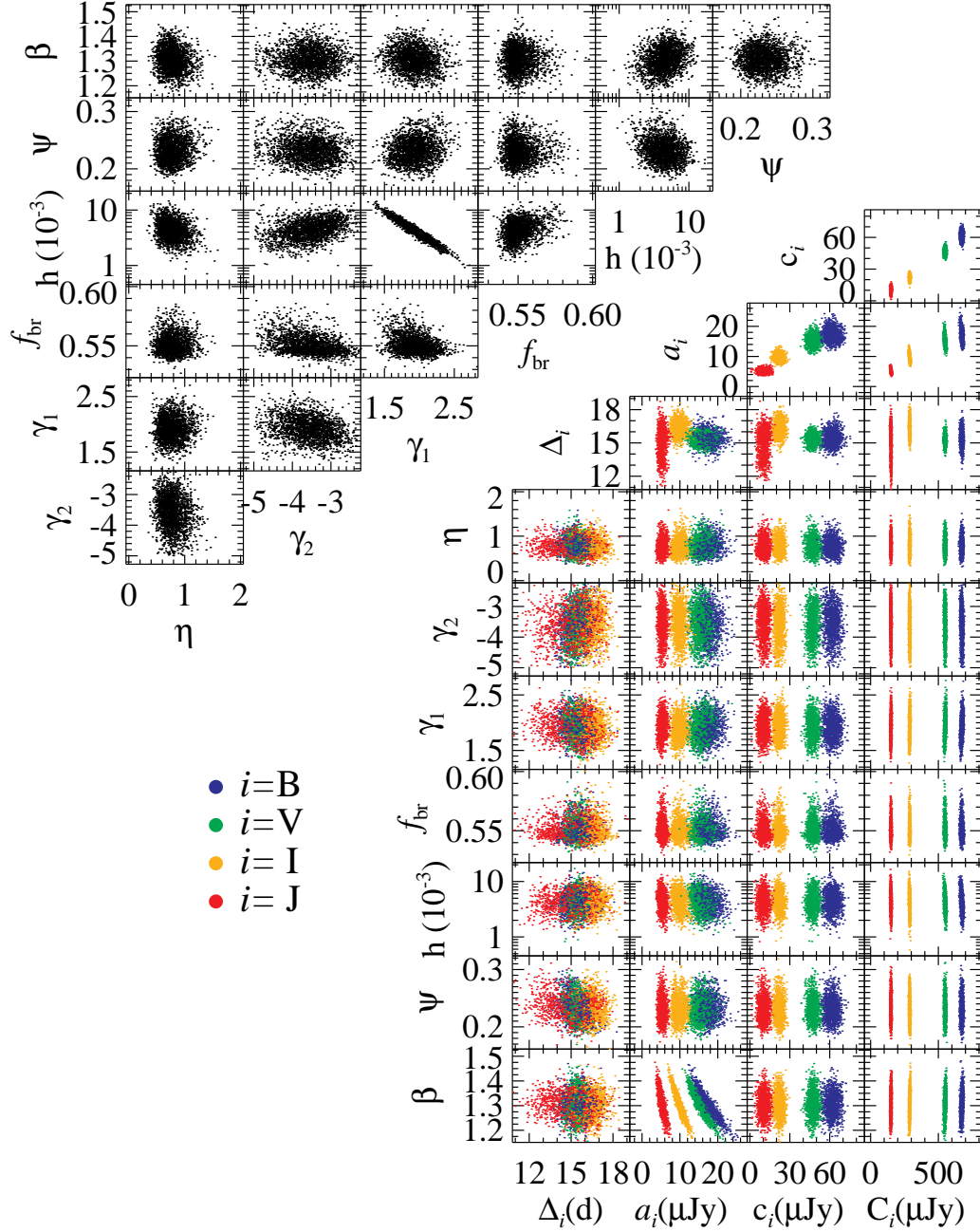


FIG. 10.— Correlations among selected fit parameters. To avoid saturating the figure, we have plotted a randomly drawn subsample of the MCMC run. Parameters which are independent for each OIR band are illustrated together in color.

Bloom, J. S., van Dokkum, P. G., Baily, C. D., Buxton, M. M., Kulkarni, S. R., & Schmidt, B. P. 2004, *AJ*, 127, 252  
 Brocksopp, C., Groot, P. J., & Wilms, J. 2001, *MNRAS*, 328, 139  
 Calvelo, D. E., Vrtillek, S. D., Steeghs, D., Torres, M. A. P., Neilsen, J., Filippenko, A. V., & González Hernández, J. I. 2009, *MNRAS*, 399, 539  
 Cambier, H. J., & Smith, D. M. 2013, *ApJ*, 767, 46  
 Chiang, E. I., & Goldreich, P. 1997, *ApJ*, 490, 368  
 Cleveland, W. S. 1979, *JASA*, 74, 829  
 Cowley, A. P., Crampton, D., Hutchings, J. B., Remillard, R., & Penfold, J. E. 1983, *ApJ*, 272, 118  
 Cowley, A. P., et al. 1991, *ApJ*, 381, 526  
 Cunningham, C. 1976, *ApJ*, 208, 534  
 Durant, M., et al. 2011, *MNRAS*, 410, 2329  
 Edelson, R. A., & Krolik, J. H. 1988, *ApJ*, 333, 646  
 Foreman-Mackey, D., Hogg, D. W., Lang, D., & Goodman, J. 2013, *PASP*, 125, 306

Frank, J., King, A., & Raine, D. J. 2002, *Accretion Power in Astrophysics* (Cambridge University Press)  
 Fukue, J. 1992, *PASJ*, 44, 663  
 Gandhi, P., et al. 2010, *MNRAS*, 407, 2166  
 Gelman, A., & Rubin, D. 1992, *Statistical Science*, 7, 457  
 Hartmann, L. 1998, *Accretion Processes in Star Formation* (Cambridge, UK, Cambridge University Press)  
 Johnston, M. D., Bradt, H. V., & Doxsey, R. E. 1979, *ApJ*, 233, 514  
 Jones, C. A., Chetin, T., & Liller, W. 1974, *ApJ*, 190, L1  
 King, A. R. 1998, *MNRAS*, 296, L45  
 King, A. R., Pringle, J. E., & Livio, M. 2007, *MNRAS*, 376, 1740  
 Kotze, M. M., & Charles, P. A. 2012, *MNRAS*, 420, 1575  
 Kubota, A., Done, C., Davis, S. W., Dotani, T., Mizuno, T., & Ueda, Y. 2010, *ApJ*, 714, 860  
 Kupfer, T., Groot, P. J., Levitan, D., Steeghs, D., Marsh, T. R., Rutten, R. G. M., & Nelemans, G. 2013, *MNRAS*, 432, 2048

- Leong, C., Kellogg, E., Gursky, H., Tananbaum, H., & Giacconi, R. 1971, *ApJ*, 170, L67
- Li, L.-X., Zimmerman, E. R., Narayan, R., & McClintock, J. E. 2005, *ApJS*, 157, 335
- Luketic, S., Proga, D., Kallman, T. R., Raymond, J. C., & Miller, J. M. 2010, *ApJ*, 719, 515
- McClintock, J. E., Shafee, R., Narayan, R., Remillard, R. A., Davis, S. W., & Li, L.-X. 2006, *ApJ*, 652, 518
- Miller, J. M., et al. 2006, *ApJ*, 646, 394
- Neilsen, J., & Homan, J. 2012, *ApJ*, 750, 27
- Neilsen, J., Steeghs, D., & Vrtilek, S. D. 2008, *MNRAS*, 384, 849
- Orosz, J., Steiner, J., McClintock, J., Buxton, M., Bailyn, C., Steeghs, D., Guberman, A., & Torres, M. 2014, *ApJ* (submitted)
- Penna, R. F., Sądowski, A., Kulkarni, A. K., & Narayan, R. 2013, *MNRAS*, 428, 2255
- Ponti, G., Fender, R. P., Begelman, M. C., Dunn, R. J. H., Neilsen, J., & Coriat, M. 2012, *MNRAS*, 422, L11
- Scargle, J. D. 1982, *ApJ*, 263, 835
- Shakura, N. I., & Sunyaev, R. A. 1973, *A&A*, 24, 337
- Smale, A. P., & Boyd, P. T. 2012, *ApJ*, 756, 146
- Song, L., et al. 2010, *AJ*, 140, 794
- Soria, R., Wu, K., Page, M. J., & Sakelliou, I. 2001, *A&A*, 365, L273
- Steeghs, D. 2004, *Astronomische Nachrichten*, 325, 185
- Steiner, J., McClintock, J., Orosz, J., Remillard, R., Bailyn, C., Kolehmainen, M., & Straub, O. 2014, *ApJ* (submitted)
- Steiner, J. F., McClintock, J. E., Remillard, R. A., Gou, L., Yamada, S., & Narayan, R. 2010, *ApJ*, 718, L117
- Steiner, J. F., Narayan, R., McClintock, J. E., & Ebisawa, K. 2009, *PASP*, 121, 1279
- Straub, O., et al. 2011, *A&A*, 533, A67
- Subasavage, J. P., Bailyn, C. D., Smith, R. C., Henry, T. J., Walter, F. M., & Buxton, M. M. 2010, in *Society of Photo-Optical Instrumentation Engineers (SPIE) Conference Series*, Vol. 7737, *Society of Photo-Optical Instrumentation Engineers (SPIE) Conference Series*
- Toor, A., & Seward, F. D. 1974, *AJ*, 79, 995
- Wen, L., Levine, A. M., Corbet, R. H. D., & Bradt, H. V. 2006, *ApJS*, 163, 372
- Wilms, J., Allen, A., & McCray, R. 2000, *ApJ*, 542, 914
- Wilms, J., Nowak, M. A., Pottschmidt, K., Heindl, W. A., Dove, J. B., & Begelman, M. C. 2001, *MNRAS*, 320, 327